

Bayesian parameter estimation on boson-star binary signals with a coherent inspiral template and spin-dependent quadrupolar corrections

Massimo Vaglio,^{1,2} Costantino Pacilio,^{3,4} Andrea Maselli,^{5,6} and Paolo Pani^{1,2}

¹*Dipartimento di Fisica, “Sapienza” Università di Roma, Piazzale Aldo Moro 5, 00185, Roma, Italy*

²*INFN, Sezione di Roma, Piazzale Aldo Moro 2, 00185, Roma, Italy*

³*Dipartimento di Fisica “G. Occhialini”, Università degli Studi di Milano-Bicocca, Piazza della Scienza 3, 20126 Milano, Italy*

⁴*INFN, Sezione di Milano-Bicocca, Piazza della Scienza 3, 20126 Milano, Italy*

⁵*Gran Sasso Science Institute (GSSI), I-67100 L’Aquila, Italy*

⁶*INFN, Laboratori Nazionali del Gran Sasso, I-67100 Assergi, Italy*

(Dated: February 28, 2023)

Compact boson star binaries are hypothetical sources for ground-based and space gravitational-wave detectors. Their signal would be a messenger for novel fundamental fields and could shed light on the dark matter. In this work, we further develop our analysis in Phys. Rev. D 102, 083002 (2020), aimed at constraining the properties of these objects with future observations. We use a coherent waveform template for the inspiral stage of boson star binaries with large quartic self interactions, including tidal deformability and the nonlinear dependence of the quadrupole moments on the spin in terms of the fundamental couplings of the scalar field theory. Performing a Bayesian analysis, we investigate the ability of a third-generation gravitational-wave detector such as the Einstein Telescope to distinguish these exotic sources from black holes and infer constraints on the fundamental couplings of the model.

I. INTRODUCTION

Boson stars (BSs) are self-gravitating condensates of a bosonic field [1–3] (see Refs. [4–6] for some reviews). Their properties such as maximum mass, radius, compactness, spin- and tidally-induced deformabilities strongly depend on the self-interactions of the underlying field theory [7–9]. Depending on the latter, BSs can exist in any mass range and can have a compactness comparable to or larger than that of a neutron star. Like standard compact objects such as neutron stars and black holes (BHs), BSs can be produced dynamically through gravitational cooling [10, 11] and can form compact binaries whose coalescence (see, e.g., [6, 12–17]) is a primary target of current and future gravitational-wave (GW) detectors [18–21]. In this context, it is intriguing that some of the detected GW events (e.g., GW190814 [22] and GW190521 [23]) might not fit naturally within the standard astrophysical formation scenarios and are compatible with more exotic origins, such as with the coalescence of two Proca stars [24], which are the vector counterparts [25] of the scalar BSs studied in this work.

Here we continue our investigation of the detectability of BS binaries with large quartic interactions [3] (sometimes called massive BSs), extending our previous studies [26, 27] in various directions. We adopt the coherent waveform template for the inspiral phase developed in Ref. [26], which is based on a TaylorF2 post-Newtonian (pN) model [28], but coherently including the spin-induced quadrupole moment [29, 30] and the tidal deformability parameters [30–32] as predicted by the scalar field theory with quartic interactions. Therefore, the waveform model depends only on the binary masses and spins, on the scalar-field mass, and on the quartic self-interaction. In the strongly-interacting limit, the latter two combine into a single parameter [26, 27], so

the waveform model contains only a single extra parameter with respect to a binary BH inspiral. Furthermore, we take advantage of our recent results for the spin-induced quadrupole moment of massive BSs [27], and include the complete nonlinear spin dependence of the 2pN phase terms in the waveform which – together with the fact that BSs have nonzero tidal deformability [7, 8] – is a key discriminator with respect to the BH case. Finally, we implement this updated waveform model into a Bayesian parameter estimation¹ using the projected sensitivity of future third-generation GW interferometers such as the Einstein Telescope (ET) [19, 34]. We show that, for typical coalescence events, ET can measure the coupling constant of the scalar-field theory with percent accuracy.

Henceforth we use $G = c = 1$ units.

II. FINITE SIZE EFFECTS FOR BOSON STAR BINARIES

Stationary axisymmetric BSs are solutions to the Einstein–Klein–Gordon equations for a complex, massive, scalar field, minimally coupled to the gravitational sector [1–3]. The theory is described by the action

$$S = \int d^4x \sqrt{-g} \left[\frac{R}{16\pi} + \mathcal{L}_\phi \right],$$

where R is the Ricci scalar, and the Lagrangian \mathcal{L}_ϕ governs the dynamics of the field ϕ . Here we consider a family of BSs characterized quartic interactions [3] (massive

¹ A similar Bayesian inference has been done in Ref. [33] using a simple polytropic perfect-fluid model to approximate a boson star and neglecting spin effects.

BSs):

$$\mathcal{L}_\phi = -\frac{1}{2}g^{\mu\nu}\phi_{,\mu}\phi_{,\nu} - \frac{1}{2}\mu^2|\phi|^2 - \frac{1}{4}\sigma|\phi|^4. \quad (1)$$

The mass parameter μ is related to the physical mass of the bosonic particle by $m_S = \hbar\mu$. We shall focus on the strong coupling limit, $\sigma \gg \mu^2$, which allows for very compact equilibrium configurations. In this limit the properties of an equilibrium configuration depend on the coupling constants μ and σ only through their combination $M_B = \sqrt{\sigma}/\mu^2$, which has dimensions of a mass [26, 27]. Moreover, we introduce the dimensionless ratio $\beta \equiv M/M_B$ (with M being the BS mass), which is convenient to parameterize the properties of the stellar structure [27, 35].

Finite-size effects related to the BS structure differ significantly from those of BHs, and introduce distinctive features within the GW signals emitted by coalescing systems, which can be exploited to disentangle the two families of compact objects. Such signatures play different roles during the inspiral stages of a binary. Far from the merger, at low frequencies, sources behave as point particles and finite size effects are effaced [36]. As the binary approaches the last phase of the coalescence, finite-size effects, induced by stellar structure, become more relevant and are strong enough to modify the system orbital evolution and its GW emission [29, 37, 38]. These modifications carry precious information on the nature of the binary components, and allow studying a variety of fundamental physics problems, from the properties of dense nuclear matter [39–41], to the nature of BHs [7, 18, 42] and their environments [43–48].

Here, adopting a pN approximation of the inspiral waveform including finite-size effects, we focus on two smoking gun signatures given by: (i) nonvanishing tidal deformabilities [7, 8] and (ii) spin induced multipole moments [26, 35] which differ from their Kerr counterparts. We model finite-size effects by additional contributions to the phase of the waveform, $\varphi = \varphi_{\text{pp}} + \varphi_{\text{T}} + \varphi_{\kappa}$, where $\varphi = \varphi_{\text{pp}}$ is the point-particle phase and φ_{T} and φ_{κ} identify the phase contributions of tidal interactions and of the spin-induced multipole moments, respectively.

As in the case of neutron-star binaries, deformations induced on BSs by the external tidal field of a companion leave a footprint on the emitted waveform encoded by the dimensionless tidal Love numbers λ_ℓ , which depend on the coupling constant of the theory and on the object's compactness [7, 8]. The leading contribution to GW emission is given by the quadrupolar coefficient λ_2 [32], which determines the dimensionless tidal deformability

$$\Lambda = \frac{2}{3}\lambda_2 \frac{R^5}{M^5} = \frac{2}{3}\lambda_2 \mathcal{C}^{-5}, \quad (2)$$

where M , R and $\mathcal{C} = M/R$ are the BS mass, radius, and compactness. The phase contribution φ_{T} depends on the tidal deformabilities $\Lambda_{1,2}$ of both binary components, and at the leading order enters the GW phase at 5pN with a

coefficient [38] (see Eq. (10) below and Appendix A)

$$\varphi_{\text{T},5} = -12[(1 + 7\eta - 31\eta^2)(\Lambda_1 + \Lambda_2) + \delta(1 + 9\eta - 11\eta^2)(\Lambda_1 - \Lambda_2)], \quad (3)$$

where $\eta = m_1 m_2 / (m_1 + m_2)^2$ is the symmetric mass ratio, $\delta = (m_1 - m_2)/m$, and $m = m_1 + m_2$ is the total mass of the binary.

A second key difference between BHs and BSs lies in their spin-induced multipolar structure. In General Relativity, stationary BHs are uniquely described by the Kerr solution, whose multipolar structure is completely determined by the mass and spin through the compact relations [49]

$$Q_\ell^{BH} + iS_\ell^{BH} = M^{\ell+1}(i\chi)^\ell, \quad (4)$$

where Q_ℓ and S_ℓ are two sets of mass and current moments, respectively, and $\chi = J/M^2$ is the BH dimensionless spin parameter, being J its angular momentum [49]. All other multipole moments vanish identically, as dictated by the axisymmetry and equatorial symmetry of the Kerr metric. For a rotating BSs, the multipole moments depend on the mass and spin but also on the scalar couplings. For example, the quadrupole moment (which is the dominant parameter, entering at 2pN order in the GW phase), can be expressed as

$$Q_2 = -\kappa_2 M^3 \chi^2, \quad (5)$$

where $\kappa_2 = \kappa_2(\chi, \beta)$. The dependence of κ_2 on the BS mass and spin, as well on the coupling parameter M_B has been investigated in details in Ref. [27]. In particular, it is found that κ_2 decreases as the BS compactness increases and, for slowly spinning configurations close to the maximum compactness, has a lower cutoff $\kappa_2 \approx 20$, to be contrasted with the BH case $\kappa_2^{BH} = 1$. Hereafter we ignore multipoles with $\ell > 2$ in the signal, focusing on the leading contribution given by the quadrupole coefficient κ_2 . The latter introduces a correction to the point-particle waveform phase which enters at 2pN order together with quadratic terms in the BS spin parameter [29, 50], with a leading-order coefficient proportional to (see Eq. (10) below and Appendix A)

$$\varphi_{\kappa,2} = -\frac{50}{m^2}(\kappa_1 m_1^2 \chi_1^2 + \kappa_2 m_2^2 \chi_2^2). \quad (6)$$

III. BINARY WAVEFORM MODEL

Our waveform model builds on the frequency-domain TaylorF2 template [28], which describes the GW inspiral signal of a binary system on quasicircular orbits,

$$\tilde{h}(f, \boldsymbol{\theta}) = \mathcal{A}(f, \boldsymbol{\theta}) e^{-i\varphi(f, \boldsymbol{\theta})}, \quad (7)$$

where f is the frequency and $\boldsymbol{\theta}$ identifies the set of source parameters. Both the amplitude and the phase of the

signal are expanded as a power series in the parameter $x = (\pi f m)^{2/3}$. A term proportional to x^n corresponds to the n -pN order of the approximation. Here we retain only the 0pN (Newtonian) term for the amplitude

$$\mathcal{A} = \mathcal{C} \sqrt{\frac{5\pi}{96}} \frac{\mathcal{M}^{5/6}}{\pi^{2/3} d_L} f^{-7/6}, \quad (8)$$

where $\mathcal{M} = (m_1 m_2)^{3/5} / m^{1/5}$ is the chirp mass, and d_L the binary luminosity distance. The geometric factor

$$\mathcal{C} = \sqrt{(1 + \cos^2 \iota)^2 F_+^2 + 4 \cos^2 \iota F_\times^2}, \quad (9)$$

depends on the antenna pattern functions $F_{+, \times} \equiv F_{+, \times}(ra, dec, \psi)$ and encodes the information about the right ascension ra and declination dec of the source, the polarization angle ψ , and the inclination angle ι between the binary orbital angular momentum and the line of sight of the source [51]. We expand the phase including contributions up to 6pN order:

$$\varphi = 2\pi f t_c - \varphi_c - \pi/4 + \frac{3}{128\eta x^{5/2}} \times \left(\sum_{i=0}^7 \varphi_{\text{pp}, i/2} x^{i/2} + \varphi_{\kappa, 2} x^2 + \varphi_{\kappa, 3} x^3 + \varphi_{\text{T}, 5} x^5 + \varphi_{\text{T}, 6} x^6 \right), \quad (10)$$

where t_c and φ_c are the time and phase at the coalescence, respectively. Specifically, we consider: (i) point particle coefficients $\varphi_{\text{pp}, i}$ including spin-orbit and spin-spin terms up to 3.5pN order [52], (ii) 2pN and 3pN spin-induced quadrupole corrections $\varphi_{\kappa, 2}$ and $\varphi_{\kappa, 3}$ as computed in [53], (iii) tidal contributions $\varphi_{\text{T}, 5}$ and $\varphi_{\text{T}, 6}$ entering at 5pN and 6pN order [54]. We refer the reader to Appendix A for their explicit form.

Ref. [8] found a simple semi-analytic expression relating $\beta = M/M_B$ to the static tidal deformability Λ , which can be inverted in the form

$$\log_{10} \Lambda = \sum_{k=0}^4 \alpha_k \beta^k, \quad (11)$$

where

$$\begin{aligned} \alpha_0 &= +7.5, & \alpha_1 &= -9.0, \\ \alpha_2 &= -4.4 \times 10^3, & \alpha_3 &= +1.0 \times 10^5, \\ \alpha_4 &= -7.7 \times 10^5. \end{aligned} \quad (12)$$

We will use this relation also for binary systems with spinning BSs, i.e. neglecting the possible (subleading) dependence of Λ on the BS spin (see Ref. [55] for an estimate of the relevance of these terms in the neutron-star case).

The BS quadrupole moment can also be determined in terms of β and of the dimensionless spin parameter χ , $\kappa_2 = \kappa_2(\beta, \chi)$, through a cubic bi-spline interpolation of the data derived in Ref. [27] on a two-dimensional (β, χ)

grid with 9×30 points in the range $0.02 \leq \beta \leq 0.06$ and $0 \leq \chi \leq 3$. The errors in the fit (11) and on the numerical interpolation of κ_2 for the tidal and quadrupole terms are discussed in Appendix B and are below 10% and 5%, respectively, within the entire grid domain.

The waveform so constructed can be fully specified by 9 intrinsic parameters and 7 extrinsic parameters. The intrinsic parameters are the chirp mass \mathcal{M} , the symmetric mass ratio η , the spin magnitudes $a_{1,2}$, the tilt angles between the spin directions and the orbital angular momentum $\theta_{1,2}$, the angle $\delta\phi$ between the two spin vectors, the angle θ_{JL} between the orbital and total angular momentum of the binary and the BS effective coupling $M_B = \sqrt{\sigma}/\mu^2$. The latter sets the mass scale for the two compact objects, and determines their tidal deformabilities and the spin-induced quadrupole moments [26, 27]. The extrinsic parameters are the sky localization angles (ra, dec) , the luminosity distance d_L , the inclination and the polarization angles (ι, ψ) , as well as the time and phase at the coalescence t_c and φ_c .

Our template is publicly available at [56, 57].

IV. PARAMETER ESTIMATION SETTINGS

We simulate injection and recovery of the waveform parameters with the open software `bilby` [58, 59]. We project the signals into a triangular ET detector with the ET-D sensitivity [34, 60] and inject the signals into white noise by adjusting the luminosity distance to the desired signal-to-noise ratio (SNR).

We expect the sky-position angles (ra, dec) , the inclination ι and the polarization angle ψ to be weakly correlated with the intrinsic parameters. Since our aim is to investigate the recovery of the BS coupling M_B and how this affects the recovery of the other intrinsic parameters, for simplicity we remove (ra, dec, ι, ψ) from the set of waveform parameters. Moreover, we focus on orbital configurations with spins (anti-)aligned with the angular momentum. Therefore, we restrict the inference to the set of parameters $\theta = \{\mathcal{M}, \eta, \chi_1, \chi_2, M_B, d_L, t_c, \phi_c\}$, where χ_i is the projection of the i -th spin along the z direction and M_B is the BS characteristic scale introduced in Sec. II. We use as injection parameters for the simulated systems the sky localization angles (ra, dec) inferred for the event GW170817 [61, 62] and we fix the inclination and polarization angles to $(\iota, \psi) = (0.4, 2.659)$. We sample the posteriors with a `dynesty` sampler using 2500 live points and we use analytic marginalization over (d_L, t_c, ϕ_c) .

Assuming Gaussian noise, the likelihood can be expressed as

$$\mathcal{L}(d|\theta) = \exp\left[-\frac{1}{2}(d - h(\theta)|d - h(\theta))\right], \quad (13)$$

where the inner product is defined by

$$(h_1, h_2) \equiv 4 \operatorname{Re} \int_{f_{\min}}^{f_{\max}} \frac{\tilde{h}_1(f) \tilde{h}_2^*(f)}{S_n(f)} df, \quad (14)$$

with $S_n(f)$ being the on one-side power spectral density. We fix the minimum frequency to $f_{\min} = 5$ Hz. The choice of the maximum frequency f_{\max} requires more care and depends on the intrinsic parameters of the injected event. Indeed, similarly to neutron stars, we need to take into account the effect of tidal deformations during the inspiral. In order to be conservative we take f_{\max} as the frequency at which the tidal force of the more compact BS overcomes the self gravity of the less compact, leading to its tidal disruption well before merger. In the Newtonian approximation, this happens when the binary orbital separation is comparable to the Roche radius [63]

$$r_{\text{Roche}} \sim \gamma r_2 \left(\frac{m_1}{m_2} \right)^{\frac{1}{3}}, \quad (15)$$

where r_2 is the radius of the secondary BS. The coefficient γ varies from the rigid body limit $\gamma = 1.26$ to the fluid body limit $\gamma = 2.44$. The corresponding Roche frequency

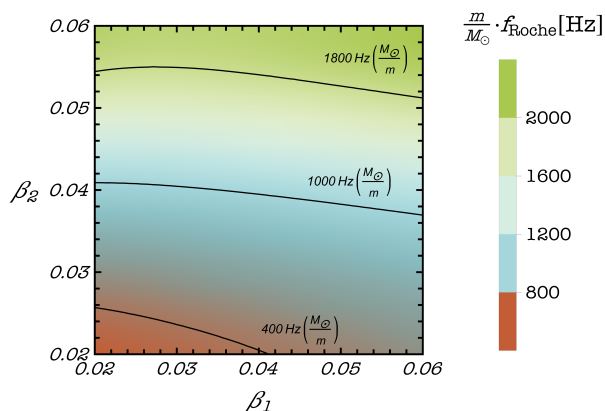


FIG. 1. Density plot showing the product $m/M_{\odot} \cdot f_{\text{Roche}}$ as a function of the rescaled masses β_1 and β_2 of the binary components. Contour lines at three different fixed values are shown as black continuous curves.

is given by

$$f_{\text{Roche}} = \frac{1}{\pi m} \sqrt{3 + q + 3q^{-1} + q^{-2}} \left(\frac{\mathcal{C}_2}{\gamma} \right)^{\frac{3}{2}}, \quad (16)$$

where $q = m_2/m_1 \leq 1$ is the mass ratio, and \mathcal{C}_2 is the compactness of the less compact star in the binary. The density plot in Fig. 1 shows values of constant $m/M_{\odot} \cdot f_{\text{Roche}}$ as a function of the rescaled masses $\beta_{i=1,2}$. Hereafter² we fix $f_{\max} = f_{\text{Roche}}$. As a further check of

the overall consistency of our framework, we have verified that, despite the large values of the tidal deformabilities Λ and of the quadrupole moments κ_2 , tidal and quadrupolar contributions to the GW phase appearing in Eq. (10), are always smaller than the Newtonian (0pN) term $\phi_{\text{pp},0} = 1$ at $f = f_{\max}$, ensuring the validity of the pN expansion. The comparison between $\varphi_{\text{T},5}$ and $\varphi_{\kappa,2}$ is shown in Fig. 2 as a function of $\beta_1 = m_1/M_B$ for different values of the mass ratio q . This comparison shows that, depending on the binary parameters, the two effects can be comparable.

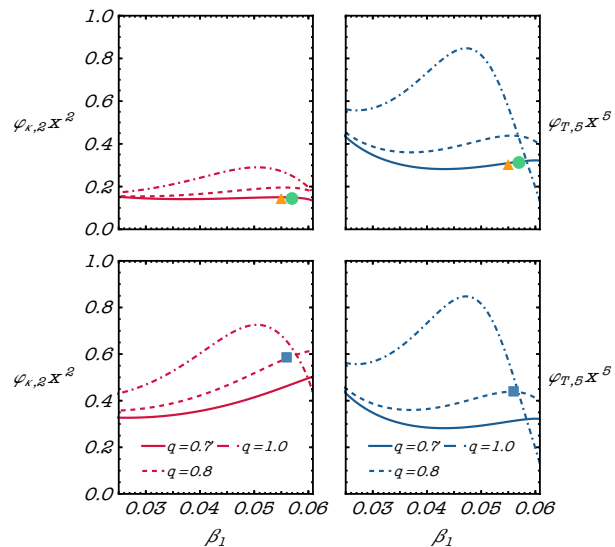


FIG. 2. Phase contribution of the leading quadrupole (2pN) and tidal (5pN) corrections normalized to the Newtonian term, evaluated at $f = f_{\text{Roche}}(\beta_1, q)$ for individual spins $\chi_1 = 0.2, \chi_2 = 0.1$ (top) and $\chi_1 = 0.05, \chi_2 = 0.35$ (bottom). The relative amplitudes are shown as functions of the primary rescaled mass $\beta_1 = m_1/M_B$ and for different values of the mass ratio q . Circle, square, and triangle dots represent the values for the first, second, and third system in Table I, respectively.

We impose flat priors on the chirp mass \mathcal{M} , the symmetric mass ratio η , the coupling M_B , and the spins χ_i within the ranges $\mathcal{M} \in [1, 25]M_{\odot}$, $\eta \in [0, 0.25]$, $M_B \in [10, 500]M_{\odot}$, and $\chi_i \in [-1, 1]$, respectively. Moreover, we require that the BS parameters $\beta_{i=1,2}$ satisfy the constraint $0.02 \leq \beta_{1,2} \leq 0.06$. The upper bound

the case in which f_{\max} is given by the contact frequency f_{contact} , defined so that the distance between the centers of the objects is equal to the sum of their radii. We also included pN corrections accounting for the tidal deformation induced on the BS shape, encoded by the superficial Love numbers [33]. For all binaries we considered, $f_{\text{contact}} > f_{\text{Roche}}$, and including higher frequencies generically improves the accuracy of the inference. We also fix $\gamma = 2.44$, being again conservative, since smaller values of γ correspond to a higher cut-off frequency.

² This is a conservative assumption. Indeed, we have also studied

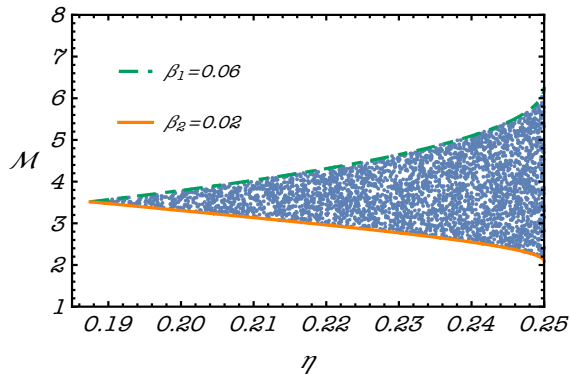


FIG. 3. Uniform sampling in the chirp mass \mathcal{M} and in the symmetric mass ratio η with constraints on the dimensionless mass parameters $0.02 < \beta_2 < \beta_1 < 0.06$ for a fixed value of $M_B = 120M_\odot$. Solid and dashed curves correspond to the upper and lower values of each component mass.

corresponds to the value of β for which the star reaches the maximum mass allowed by the model for static stellar configurations [3, 26], while the lower edge is chosen to exclude stellar configurations which are too diluted. Indeed, for $\beta \lesssim 0.02$, the BS compactness drops to³ $\mathcal{C} \lesssim 0.035$, much less compact than a typical neutron star. The constraints on $\beta_{1,2}$ introduce a nontrivial dependence on the joint prior distribution of \mathcal{M} and η . This is clear in Fig. 3 which shows how the uniform sampling in the (\mathcal{M}, η) plane is cut by our prior assumption on β , for a representative value of M_B .

V. RESULTS

We show here the results of our parameter estimation for three representative binary BS systems with properties listed in Table I, the first two having $\mathcal{M} = 5M_\odot$ and the third one with $\mathcal{M} = 10M_\odot$. The first and third systems share the same values of (η, χ_1, χ_2) , while the

second system has a higher value of the mass ratio and different spin components. The value of M_B for each system is chosen in such a way to have β_1 close to the upper limit $\beta_{\max} = 0.06$, so the primary BS is near its maximum compactness.

To compare the results, we choose the luminosity distance d_L such that $\text{SNR} \sim 130$ for all systems. The values reported for the component masses, the chirp mass, and the coupling M_B are all expressed in the detector frame⁴.

$(m_1, m_2) [M_\odot]$	(β_1, β_2)	η	$M_B [M_\odot]$	χ_1	χ_2
(6.9, 4.8)	(0.057, 0.040)	0.242	120	0.20	0.10
(6.4, 5.2)	(0.056, 0.045)	0.247	115	0.05	0.35
(13.8, 9.6)	(0.055, 0.039)	0.242	250	0.20	0.10

TABLE I. Intrinsic parameters of the injected signals.

The corner plots in Fig. 4 show the reconstructed posterior distributions, together with the injected values, for the intrinsic parameters of the two lower-mass binaries in Table I. The two-dimensional posteriors highlight a correlation between the symmetric mass ratio η and the coupling M_B . This might be related to a correlation between M_B and β_2 and to its anti-correlation with β_1 . The inferred values of the parameters (90% confidence interval) are reported in Table II. As expected the chirp mass and the symmetric mass ratio are the best recovered parameters, but it is interesting that the BS coupling M_B can be measured at the percent level, significantly better than the individual spins.

The results of the parameter estimation for the third system are shown in Fig. 5. This source has a larger chirp mass and a smaller Roche frequency ($f_{\text{Roche}} \approx 45\text{Hz}$), so the binary performs less cycles in the detector bandwidth. Correspondingly, we expect a worse recovery of the binary parameters. Indeed, the chirp mass is measured with larger uncertainty compared to the two systems with $\mathcal{M} = 5M_\odot$, and error on the primary spin is roughly doubled compared to the first system. Interestingly, M_B is still measured with very good accuracy, with relative errors below 3%. Overall, our results for the Bayesian inference are in good agreement with the estimates in [26] based on a Fisher matrix analysis.

$(m_1, m_2) [M_\odot]$	$d_L [\text{Mpc}]$	$f_{\text{Roche}} [\text{Hz}]$	$\mathcal{M} [M_\odot]$	η	$M_B [M_\odot]$	$\delta M_B [\%]$	χ_1	$\delta \chi_1 [\%]$	χ_2	$\delta \chi_2 [\%]$
(6.9, 4.8)	610	100	(4.9999, 5.0006)	(0.241, 0.249)	(118.5, 122.2)	1.5%	(0.13, 0.32)	50%	(-0.01, 0.28)	131%
(6.4, 5.2)	600	127	(4.9995, 5.0005)	(0.244, 0.250)	(113.2, 116.4)	1.5%	(0.02, 0.42)	285%	(-0.09, 0.40)	79%
(13.8, 9.6)	1150	45	(9.999, 10.011)	(0.237, 0.249)	(241.5, 253.9)	2.5%	(0.14, 0.54)	83%	(-0.02, 0.41)	134%

TABLE II. 90% confidence intervals (CI) and relative percentage errors, expressed as the half-width of the CI with respect to the median of the distribution, for the recovered parameters of the three systems in Table I.

³ Such lower value of \mathcal{C} holds for static configurations, although slowly spinning BSs feature a similar bound [35].

⁴ Notice that because both m_i and M_B are given in the detector

frame, their ratio β_i is redshift-independent, and so are dimensionless quantities such as $\Lambda(\beta)$ and $\kappa_2(\beta, \chi)$.

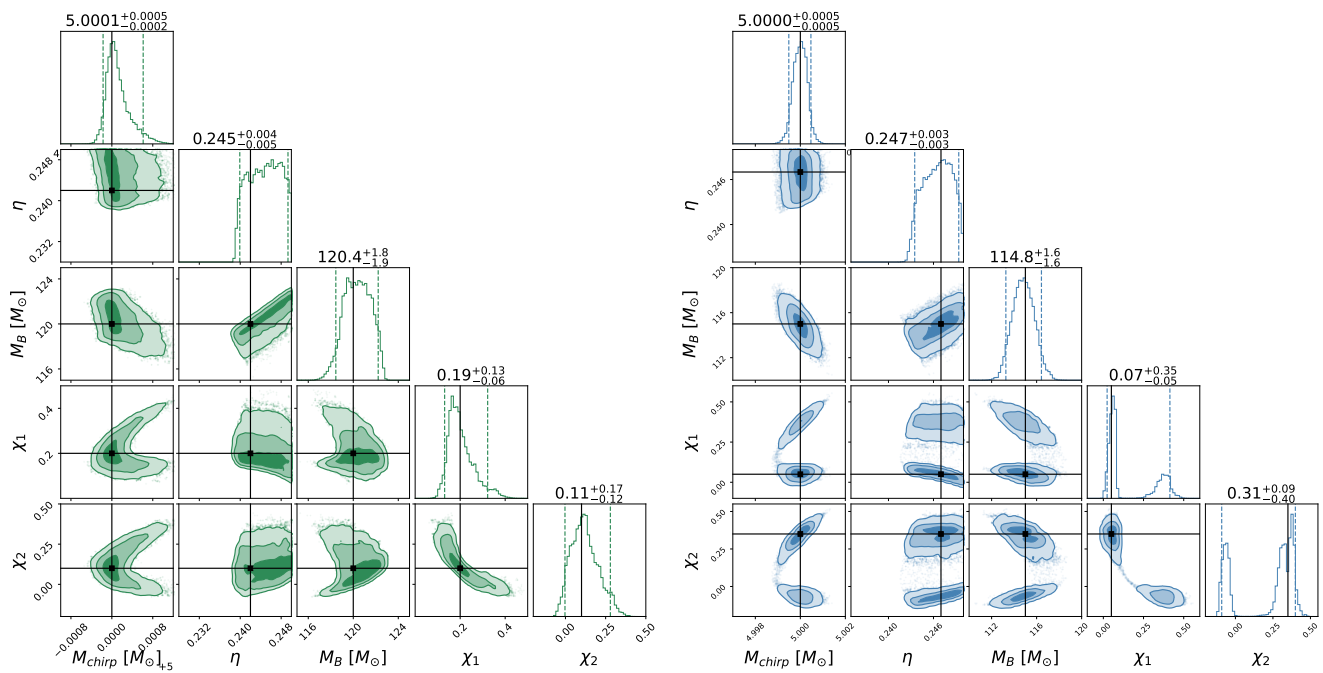


FIG. 4. Contour plots for the recovered posterior distributions of two BS binary signals corresponding to the first two configurations shown in Table I. Both systems have injected chirp mass $\mathcal{M} = 5M_\odot$, and SNR ~ 130 . (Left panel) The injected signal has $\eta = 0.2423$ ($q \sim 0.7$), $M_B = 115M_\odot$ and $(\chi_1, \chi_2) = (0.2, 0.1)$. (Right panel) The injected signal has $\eta = 0.247$ ($q \sim 0.8$), $M_B = 115M_\odot$ and $(\chi_1, \chi_2) = (0.05, 0.35)$. A secondary peak, roughly in correspondence of the injected value for the other spin component, is evident in the posterior distributions for both χ_1 and χ_2 (see discussion below).

A novel effect which emerges from the full Bayesian approach is that, for certain systems and choices of χ_1 and χ_2 , there are degeneracies among different spin configurations and multipeak posteriors, which worsen the overall recovery. This effect appears to be more relevant for nearly symmetric binaries with moderate or high values of one of the spin components (or both) for which the *sign* of the antisymmetric spin combination, $\chi_a/|\chi_a|$, is poorly measured. Indeed, in the equal mass case χ_a is completely undetermined as it only enters in the waveform through quadratic combinations, χ_a^2 , or in products $(\chi_1 + \chi_2)(\kappa_2^1 - \kappa_2^2)\chi_a$, both invariant under the exchange $\chi_1 \leftrightarrow \chi_2$. This leads to two peaks in the posterior spin distributions, associated to the two possible signs $\chi_a = \pm|\chi_a|$.

A representative example of these secondary peaks is contained in the right corner plot in Fig 4, which displays the marginalized posterior distribution of the individual spins for the second system in Table I, having $\eta = 0.247$ ($q = 0.8$) and $\chi_1 = 0.05$, $\chi_2 = 0.35$. Although the injected parameters fall within the recovered posteriors, a small secondary peak in the distribution of χ_1 contributes to a increase the error, while a higher one is also evident in the distribution of χ_2 . For fixed spin configurations, the bimodal feature is softened and tends to disappear for low mass ratios and high SNR.

Excluding situations where such degeneracy is present, we found that including quadrupolar corrections gener-

ically improves the parameter estimation. Indeed, although the constraints on M_B come mostly from the tidal deformability contribution, overall the errors on all parameters increase when setting the quadrupole corrections to zero. The reconstruction of χ_1 and χ_2 is, as expected, the most affected and their uncertainty typically increases by a factor of ~ 4 when only including point-particle terms up to $3.5pN$ and tidal corrections. Furthermore we point out that neglecting the quadrupole moment in the recovery leads to biases in the measurement of the parameters if the signal is injected using the full waveform template. Figure 6 shows this case for three different binaries, respectively corresponding to: the first and third systems in Table I and a system having $\mathcal{M} = 10M_\odot$ (i.e. with the same chirp mass of our third system) but intermediate spins, $(\chi_1, \chi_2) = (0.4, 0.7)$. The estimated value of the chirp mass is always biased, the bias being more relevant for the low-mass (panel a) and intermediate-spin (panel c) systems. In the first case this is due to the overall better accuracy in the recovery. In the case of system (c) the higher values of the spins imply larger quadrupolar corrections (consistent with the bottom panels of Fig. 2) and thus a larger departure from the original signal when neglecting them. The bias on M_B is weaker but still relevant for systems (a) and (c), while the inferred values of M_B for system (b) are fully compatible in the two cases.

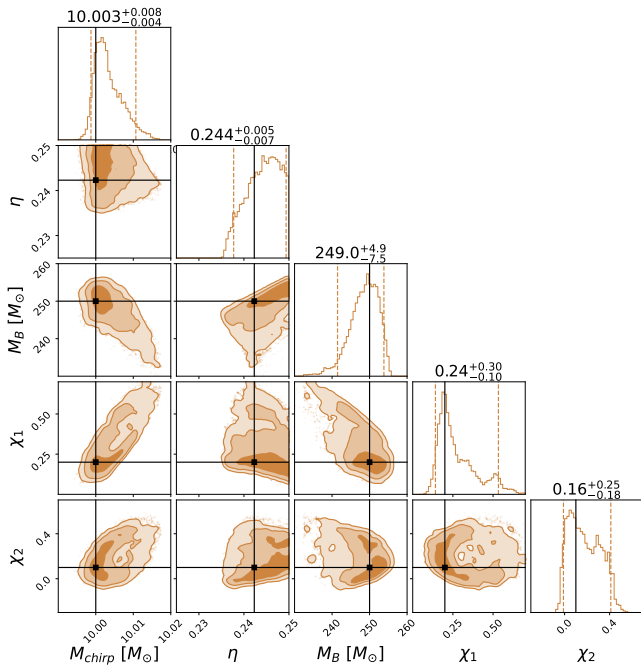


FIG. 5. Same as Fig. 4 but for the third system in Table I, with a chirp mass $\mathcal{M} = 10M_\odot$.

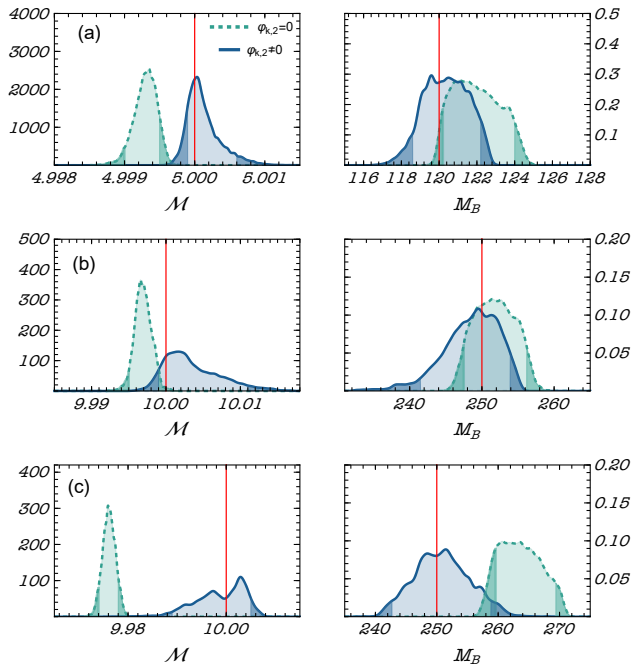


FIG. 6. Posterior distributions of \mathcal{M} (left panels) and M_B (right panels) for different systems, obtained fixing $\varphi_{2,\kappa} = 0$ in the recovery (dashed) or using the full template (solid). The injected values are identified by a vertical red line while CI of 90% are marked by a change in the curve filling. The considered systems are: (a) the first system in Table I, (b) the third system in Table I, (c) the same system as in (b) but with intermediate spins $(\chi_1, \chi_2) = (0.4, 0.7)$

VI. DISCUSSION AND CONCLUSIONS

We have presented the first Bayesian inference on BS binaries with large self interactions using a coherent inspiral template. Compared to the standard binary BH case, this template contains an extra parameter that regulates both the tidal deformability and the spin-induced quadrupole moment in terms of the masses and spins of the binary components.

Making a conservative assumption and cutting the signal at the threshold for tidal disruption, we found that future third-generation detectors such as ET can measure the BS coupling constant at the percent level. The best constraints come from binaries with relatively small chirp mass, which are also those for which the inspiral-only template is more relevant.

Overall, we confirm the estimates in Ref. [26] obtained by a Fisher-matrix analysis and with an approximated spin-induced quadrupole moment. Using the corroborated estimates of Ref. [26] as a guide, we expect the same percent accuracy in measuring M_B also with the future space mission LISA [20, 21] but for BSs with masses around $10^5 M_\odot$ (corresponding to $M_B \approx (10^5 - 10^6) M_\odot$) at a luminosity distance of 10 Gpc.

Given the relatively small cut-off frequency, the accuracy of this measurement relies on ET sensitivity around and below 100 Hz and it would quickly deteriorate for current detectors. Nevertheless, it might be interesting to apply our template to real LIGO-Virgo-KAGRA data, also comparing the Bayesian evidence for the BS model with that for a standard BH binary inspiral. Along this line – and since our template is based on the TaylorF2 approximant and therefore valid only in the inspiral phase – natural extensions of our work include using this template to inform effective inspiral-merger-ringdown models [64] or to extend merger waveforms obtained from numerical-relativity simulations [6, 12–17] (as in the recent case of Proca star head-on collisions [65] and the subsequent Bayesian inference [66]). Another possibility would be extending the waveform using effective models with frequency-dependent tidal deformability terms, as recently done in Ref. [48].

ACKNOWLEDGMENTS

Numerical calculations have been performed at the CINECA Marconi cluster through a CINECA-INFN agreement. P.P. acknowledge financial support provided under the European Union’s H2020 ERC, Starting Grant agreement no. DarkGRA–757480 and under the MIUR PRIN programme, and support from the Amaldi Research Center funded by the MIUR program “Dipartimento di Eccellenza” (CUP: B81I18001170001). C.P. is supported by European Union’s H2020 ERC Starting Grant No. 945155–GWmining and by Cariplo Foundation Grant No. 2021-0555.

Appendix A: Waveform phase coefficients

Here we show the explicit expressions of the pN coefficients of the waveform phase expansion of Eq. (10) in terms of the masses m_i , the dimensionless spins $\chi_i = J_i/M_i^2$, the tidal deformabilities $\Lambda_i = (2/3)\lambda_2^i C_i^{-5}$ and the reduced quadrupole moments $\kappa_2^i = Q_i/(\chi_i^2 m_i^3)$.

The non-zero coefficients are listed below, where

the following quantities have been introduced

$$\begin{aligned} m &= m_1 + m_2 & \eta &= m_1 m_2 / M^2 \\ \delta &= (m_1 - m_2) / M & \chi_{s/a} &= (\chi_1 \pm \chi_2) / 2 \\ \Lambda_{s/a} &= (\Lambda_1 \pm \Lambda_2) / 2 & \kappa_{s/a} &= (\kappa_2^1 \pm \kappa_2^2) / 2 \\ \gamma_E &= 0.5772156649. \end{aligned}$$

We considered spin-spin and spin-orbit corrections up to second order in the spin.

$$\begin{aligned} \varphi_{\text{pp},0} &= 1 \\ \varphi_{\text{pp},0.5} &= 0 \\ \varphi_{\text{pp},1} &= \frac{3715}{756} + \frac{55\eta}{9} \\ \varphi_{\text{pp},1.5} &= -16\pi + \frac{113}{3}\delta\chi_a + \left(\frac{113}{3} - \frac{76\eta}{3}\right)\chi_s \\ \varphi_{\text{pp},2} &= \frac{15293365}{508032} + \frac{27145\eta}{504} + \frac{3085\eta^2}{72} - \frac{5}{8}\chi_s^2(1 + 156\eta) + \chi_a^2\left(-\frac{5}{8} + 100\eta\right) - \frac{5}{4}\chi_a\chi_s\delta, \\ \varphi_{\text{pp},2.5} &= [1 + \log(\pi M f)] \left[\frac{38645\pi}{756} - \frac{65\pi\eta}{9} + \delta\left(-\frac{732985}{2268} - \frac{140\eta}{9}\right)\chi_a + \left(-\frac{732985}{2268} + \frac{24260\eta}{81} + \frac{340\eta^2}{9}\right)\chi_s \right] \\ \varphi_{\text{pp},3} &= \frac{11583231236531}{4694215680} - \frac{6848\gamma_E}{21} - \frac{640\pi^2}{3} + \left(-\frac{15737765635}{3048192} + \frac{2255\pi^2}{12}\right)\eta + \frac{76055\eta^2}{1728} - \frac{127825\eta^3}{1296} \\ &\quad - \frac{6848}{63}\log(64\pi M f) + \pi \left[\frac{2270}{3}\delta\chi_a + \left(\frac{2270}{3} - 520\eta\right)\chi_s \right] \\ &\quad + \chi_s^2\left(-\frac{1344475}{2016} + \frac{829705}{504}\eta + \frac{3415}{9}\eta^2\right) + \chi_a^2\left(-\frac{1344475}{2016} + \frac{267815}{252}\eta - 240\eta^2\right) + \chi_a\chi_s\delta\left(-\frac{1344475}{1008} + \frac{745}{18}\eta\right) \\ \varphi_{\text{pp},3.5} &= \frac{77096675\pi}{254016} + \frac{378515\pi\eta}{1512} - \frac{74045\pi\eta^2}{756} + \left(-\frac{25150083775}{3048192} + \frac{26804935}{6048}\eta - \frac{1985}{48}\eta^2\right)\delta\chi_a \\ &\quad + \left(-\frac{25150083775}{3048192} + \frac{10566655595}{762048}\eta - \frac{1042165}{3024}\eta^2 + \frac{5345}{36}\eta^3\right)\chi_s \\ \varphi_{\kappa,2} &= -\frac{5}{8}\chi_s^2[80\delta\kappa_a + 80(1 - 2\eta)\kappa_s] + \chi_a^2[-50\delta\kappa_a - 50\kappa_s + 100\eta\kappa_s] - \frac{5}{4}\chi_a\chi_s[80(1 - 2\eta)\kappa_a + 80\delta\kappa_s], \\ \varphi_{\kappa,3} &= (\chi_s^2 + \chi_a^2) \left[\delta\left(\frac{26015}{28} - \frac{1495}{6}\eta\right)\kappa_a + \left(\frac{26015}{28} - \frac{44255}{21}\eta - 240\eta^2\right)\kappa_s \right] \\ &\quad + \chi_a\chi_s \left[\left(\frac{26015}{14} - \frac{88510}{21}\eta - 480\eta^2\right)\kappa_a + \delta\left[\left(\frac{26015}{14} - \frac{1495}{3}\eta\right)\kappa_s\right] \right] \\ \varphi_{\text{T},5} &= -24[(1 + 7\eta - 31\eta^2)\Lambda_s + \delta(1 + 9\eta - 11\eta^2)\Lambda_a], \\ \varphi_{\text{T},6} &= -\frac{3115}{52}[(1 + 7\eta - 31\eta^2)\Lambda_s + \delta(1 + 9\eta - 11\eta^2)\Lambda_a] \\ &\quad + \frac{6595}{364}\delta\left[\delta\left(1 - \frac{13272}{1319}\eta + \frac{8944}{1319}\eta^2\right)\Lambda_s + \left(1 - \frac{15910}{1319}\eta + \frac{32850}{1319}\eta^2 + \frac{3380}{1319}\eta^3\right)\Lambda_a\right]. \end{aligned}$$

Appendix B: On the $\Lambda(\beta)$ and $\kappa_2(\chi, \beta)$ relations

To obtain the tidal deformability we inverted the relation for $\beta(\Lambda)$ provided in Ref. [8], for which the authors estimate an error of the order of 1%. However, the error on the inverse can be higher, especially close to the sta-

tionary point at $\beta \approx 0.06011$, where the first derivative of the inverse function formally diverges. Neglecting the error introduced in numerically evaluating the inverse, we can simply consider the propagation of the relative

error on β :

$$\delta_{\text{rel}}\Lambda = \frac{\beta \cdot \Lambda'(\beta)}{\Lambda(\beta)} \delta_{\text{rel}}\beta$$

Applying this relation, the error on Λ is below 10% for $\beta \leq 0.057$, which is saturated by the higher β considered for the primary object in the main text. The stationary point is excluded even from the sampling because of the constraint $\beta \leq 0.06$.

To obtain the reduced quadrupole moment $\kappa_2(\chi, \beta)$ we interpolated the data in [27] on a bi-dimensional grid $n_\beta \times n_\chi = 9 \times 30$, using cubic splines. An error bound for cubic spline interpolation is provided in Ref. [67]

$$\delta s = |f - s| \sim \frac{3}{154} |f^{(4)}| h^4 \sim \frac{3}{154} \left| \frac{s''_{i+1} - 2s''_i + s''_{i-1}}{h^2} \right| h^4$$

where s is the spline interpolation function, s''_i its second derivative at a given grid point and h the grid spacing. We used equally-spaced grid points in β and in the logarithm of the spin, $\log(\chi)$. We can apply the formula separately for the interpolation in β and χ , using $h_\beta = \beta_{i+1} - \beta_i$ and $h_\chi = \log(\chi_{i+1}) - \log(\chi_i)$. We found that the errors are of the order of 1% and 5% in the β and χ direction, respectively. For spin larger than $\chi \sim 0.1$, this will be the dominant contribution to the total uncertainty on the reduced quadrupole κ_2 , while for smaller χ , it will be dominated by the numerical error on the data, which can reach the order of 10% for such small spin values [27].

-
- [1] D. J. Kaup, *Phys. Rev.* **172**, 1331 (1968).
[2] R. Ruffini and S. Bonazzola, *Phys. Rev.* **187**, 1767 (1969).
[3] M. Colpi, S. L. Shapiro, and I. Wasserman, *Phys. Rev. Lett.* **57**, 2485 (1986).
[4] P. Jetzer, *Phys. Rept.* **220**, 163 (1992).
[5] F. E. Schunck and E. W. Mielke, *Class. Quant. Grav.* **20**, R301 (2003), arXiv:0801.0307 [astro-ph].
[6] S. L. Liebling and C. Palenzuela, *Living Rev. Rel.* **15**, 6 (2012), arXiv:1202.5809 [gr-qc].
[7] V. Cardoso, E. Franzin, A. Maselli, P. Pani, and G. Raposo, *Phys. Rev. D* **95**, 084014 (2017), [Addendum: *Phys.Rev.D* 95, 089901 (2017)], arXiv:1701.01116 [gr-qc].
[8] N. Sennett, T. Hinderer, J. Steinhoff, A. Buonanno, and S. Ossokine, *Phys. Rev. D* **96**, 024002 (2017), arXiv:1704.08651 [gr-qc].
[9] M. Bošković and E. Barausse, *JCAP* **02** (02), 032, arXiv:2111.03870 [gr-qc].
[10] E. Seidel and W.-M. Suen, *Phys. Rev. Lett.* **72**, 2516 (1994), arXiv:gr-qc/9309015.
[11] F. Di Giovanni, N. Sanchis-Gual, C. A. Herdeiro, and J. A. Font, *Phys. Rev. D* **98**, 064044 (2018), arXiv:1803.04802 [gr-qc].
[12] C. Palenzuela, L. Lehner, and S. L. Liebling, *Phys. Rev. D* **77**, 044036 (2008), arXiv:0706.2435 [gr-qc].
[13] C. Palenzuela, P. Pani, M. Bezares, V. Cardoso, L. Lehner, and S. Liebling, *Phys. Rev. D* **96**, 104058 (2017), arXiv:1710.09432 [gr-qc].
[14] M. Bezares, C. Palenzuela, and C. Bona, *Phys. Rev. D* **95**, 124005 (2017), arXiv:1705.01071 [gr-qc].
[15] N. Sanchis-Gual, C. Herdeiro, J. A. Font, E. Radu, and F. Di Giovanni, *Phys. Rev. D* **99**, 024017 (2019), arXiv:1806.07779 [gr-qc].
[16] M. Bezares, M. Bošković, S. Liebling, C. Palenzuela, P. Pani, and E. Barausse, *Phys. Rev. D* **105**, 064067 (2022), arXiv:2201.06113 [gr-qc].
[17] N. Siemonsen and W. E. East, (2023), arXiv:2302.06627 [gr-qc].
[18] V. Cardoso and P. Pani, *Living Rev. Rel.* **22**, 4 (2019), arXiv:1904.05363 [gr-qc].
[19] M. Maggiore *et al.*, *JCAP* **03**, 050, arXiv:1912.02622 [astro-ph.CO].
[20] K. G. Arun *et al.* (LISA), *Living Rev. Rel.* **25**, 4 (2022), arXiv:2205.01597 [gr-qc].
[21] E. Barausse *et al.*, *Gen. Rel. Grav.* **52**, 81 (2020), arXiv:2001.09793 [gr-qc].
[22] R. Abbott *et al.* (LIGO Scientific, Virgo), *Astrophys. J. Lett.* **896**, L44 (2020), arXiv:2006.12611 [astro-ph.HE].
[23] R. Abbott *et al.* (LIGO Scientific, Virgo), *Phys. Rev. Lett.* **125**, 101102 (2020), arXiv:2009.01075 [gr-qc].
[24] J. Calderón Bustillo, N. Sanchis-Gual, A. Torres-Forné, J. A. Font, A. Vajpeyi, R. Smith, C. Herdeiro, E. Radu, and S. H. W. Leong, *Phys. Rev. Lett.* **126**, 081101 (2021), arXiv:2009.05376 [gr-qc].
[25] R. Brito, V. Cardoso, C. A. R. Herdeiro, and E. Radu, *Phys. Lett. B* **752**, 291 (2016), arXiv:1508.05395 [gr-qc].
[26] C. Pacilio, M. Vaglio, A. Maselli, and P. Pani, *Phys. Rev. D* **102**, 083002 (2020), arXiv:2007.05264 [gr-qc].
[27] M. Vaglio, C. Pacilio, A. Maselli, and P. Pani, *Phys. Rev. D* **105**, 124020 (2022), arXiv:2203.07442 [gr-qc].
[28] T. Damour, B. R. Iyer, and B. S. Sathyaprakash, *Phys. Rev. D* **63**, 044023 (2001), [Erratum: *Phys.Rev.D* 72, 029902 (2005)], arXiv:gr-qc/0010009.
[29] E. Poisson, *Physical Review D* **57**, 5287 (1998).
[30] E. Poisson and C. Will, *Gravity: Newtonian, Post-Newtonian, Relativistic* (Cambridge University Press, Cambridge, UK, 1953).
[31] E. E. Flanagan and T. Hinderer, *Phys. Rev. D* **77**, 021502 (2008), arXiv:0709.1915 [astro-ph].
[32] T. Hinderer, *Astrophys. J.* **677**, 1216 (2008), arXiv:0711.2420 [astro-ph].
[33] N. K. Johnson-Mcdaniel, A. Mukherjee, R. Kashyap, P. Ajith, W. Del Pozzo, and S. Vitale, *Phys. Rev. D* **102**, 123010 (2020), arXiv:1804.08026 [gr-qc].
[34] S. Hild *et al.*, *Class. Quant. Grav.* **28**, 094013 (2011), arXiv:1012.0908 [gr-qc].
[35] F. D. Ryan, *Phys. Rev. D* **55**, 6081 (1997).
[36] L. Blanchet, *Living Reviews in Relativity* **17**, 2 (2014).
[37] T. Hinderer, B. D. Lackey, R. N. Lang, and J. S. Read, *Physical Review D* **81**, 123016 (2010), arXiv:0911.3535 [astro-ph, physics:gr-qc].
[38] M. Favata, *Phys. Rev. Lett.* **112**, 101101 (2014), arXiv:1310.8288 [gr-qc].
[39] A. Maselli, L. Gualtieri, and V. Ferrari, *Physical Review D* **88**, 104040 (2013), arXiv:1310.5381 [astro-ph,

- physics:gr-qc].
- [40] M. Agathos, J. Meidam, W. Del Pozzo, T. Li, M. Tompitak, J. Veitch, S. Vitale, and C. Van Den Broeck, *Physical Review D* **92**, 023012 (2015).
- [41] K. Chatziioannou, *General Relativity and Gravitation* **52**, 109 (2020), arXiv:2006.03168 [astro-ph, physics:gr-qc, physics:nucl-th].
- [42] L. Barack *et al.*, *Class. Quant. Grav.* **36**, 143001 (2019), arXiv:1806.05195 [gr-qc].
- [43] C. F. B. Macedo, P. Pani, V. Cardoso, and L. C. B. Crispino, *Astrophys. J.* **774**, 48 (2013), arXiv:1302.2646 [gr-qc].
- [44] E. Barausse, V. Cardoso, and P. Pani, *Phys. Rev. D* **89**, 104059 (2014), arXiv:1404.7149 [gr-qc].
- [45] V. Cardoso and A. Maselli, *Astron. Astrophys.* **644**, A147 (2020), arXiv:1909.05870 [astro-ph.HE].
- [46] V. Cardoso and F. Duque, *Phys. Rev. D* **101**, 064028 (2020), arXiv:1912.07616 [gr-qc].
- [47] V. De Luca and P. Pani, *JCAP* **08**, 032, arXiv:2106.14428 [gr-qc].
- [48] V. De Luca, A. Maselli, and P. Pani, (2022), arXiv:2212.03343 [gr-qc].
- [49] R. O. Hansen, *Journal of Mathematical Physics* **15**, 46 (1974).
- [50] L. Barack and C. Cutler, *Physical Review D* **75**, 042003 (2007).
- [51] B. F. Schutz and M. Tinto, *Monthly Notices of the Royal Astronomical Society* **224**, 131 (1987).
- [52] S. Khan, S. Husa, M. Hannam, F. Ohme, M. Pürrer, X. Jiménez Forteza, and A. Bohé, *Phys. Rev. D* **93**, 044007 (2016), arXiv:1508.07253 [gr-qc].
- [53] N. V. Krishnendu, K. G. Arun, and C. K. Mishra, *Phys. Rev. Lett.* **119**, 091101 (2017), arXiv:1701.06318 [gr-qc].
- [54] B. D. Lackey and L. Wade, *Phys. Rev. D* **91**, 043002 (2015), arXiv:1410.8866 [gr-qc].
- [55] G. Castro, L. Gualtieri, A. Maselli, and P. Pani, *Phys. Rev. D* **106**, 024011 (2022), arXiv:2204.12510 [gr-qc].
- [56] (), <https://web.uniroma1.it/gmunu/>.
- [57] (), <https://github.com/masellia/SGREP/>.
- [58] G. Ashton *et al.*, *Astrophys. J. Suppl.* **241**, 27 (2019), arXiv:1811.02042 [astro-ph.IM].
- [59] I. M. Romero-Shaw *et al.*, *Mon. Not. Roy. Astron. Soc.* **499**, 3295 (2020), arXiv:2006.00714 [astro-ph.IM].
- [60] S. Hild, S. Chelkowski, A. Freise, J. Franc, N. Morgado, R. Flaminio, and R. DeSalvo, *Classical and Quantum Gravity* **27**, 015003 (2010), arXiv:0906.2655 [gr-qc].
- [61] B. P. Abbott *et al.* (LIGO Scientific, Virgo), *Phys. Rev. X* **9**, 011001 (2019), arXiv:1805.11579 [gr-qc].
- [62] D. A. Coulter *et al.*, *Science* **358**, 1556 (2017), arXiv:1710.05452 [astro-ph.HE].
- [63] E. Roche, *La figure d'une masse fluide soumise à l'attraction d'un point éloigné*, 1st ed. (Académie des sciences de Montpellier: Mémoires de la section des sciences, 1849).
- [64] A. Toubiana, S. Babak, E. Barausse, and L. Lehner, *Phys. Rev. D* **103**, 064042 (2021), arXiv:2011.12122 [gr-qc].
- [65] N. Sanchis-Gual, J. Calderón Bustillo, C. Herdeiro, E. Radu, J. A. Font, S. H. W. Leong, and A. Torres-Forné, *Phys. Rev. D* **106**, 124011 (2022), arXiv:2208.11717 [gr-qc].
- [66] J. Calderon Bustillo, N. Sanchis-Gual, S. H. W. Leong, K. Chandra, A. Torres-Forne, J. A. Font, C. Herdeiro, E. Radu, I. C. F. Wong, and T. G. F. Li, arXiv e-prints, arXiv:2206.02551 (2022), arXiv:2206.02551 [gr-qc].
- [67] C. A. Hall and W. Meyer, *Journal of Approximation Theory* **16**, 105 (1976).